Chapter - 2
Main Problems of Creation Laser-Induced Thin Films

<u>**Author**</u>

Petro P. Trokhimchuck

Anatoliy Svidznskii, Department of the Theoretical and Computer Physics, Lesya Ukrayinka Volyn National University, Voly av., 13, Lutsk, Ukraine

Chapter - 2

Main Problems of Creation Laser-Induced Thin Films

Petro P. Trokhimchuck

Abstract

Main peculiarities of generation and modeling of laser-induced films are discussing. This problem is connecting with problem of phase transformations. Difference mechanisms of generation surface and subsurface laser-induced structures are analyzing. Roles of regimes of irradiation (saturation of excitation, geometrical sizes of irradiation zone, temporal characteristics) on formation corresponding structures and geometrical form of substrate are shown. So, the surface laser-induced structures are represented of indium antimonite, indium arsenide, silicon and germanium structures, which are received after irradiation of nanosecond pulses of Neodimium laser and nanosecond and millisecond Ruby laser. Volume structures are represented for femtosecond pulse laser irradiation of silicon carbide and nanosecond pulse CO_2-laser irradiation of potassium chloride. Two various models allow to explain these results. Some problems of application these results in modern optoelectronics in more wide sense (including other methods of receiving black silicon and other nanostructures) are discussing too.

Keywords: Laser, thin films, relaxed optics, indium antimonite, silicon carbide, chain processes, black nsilicon

Introduction

The problem of using the lasser radiation in technology of thin films may be classifing in next time [1- 33]:

1. Using the laser radiation for sputtering of irradiated material and applying it to a suitable substrate in a vacuum. The thickness of the applied film depends on the intensity and time of irradiation. The process itself has an orientation character [1-11, 15-19].
2. Laser implantation, that is, a change in the physical parameters of the irradiated material in the near-surface area, although volume changes can also be obtained [1-4, 12-14, 20-28, 33].

3. Other various complex treatments, including laser annealing of ion-implanted layers of semiconductor materials, photolithography, etc [15, 16, 29-32].

For all these three cases, we must take into account the physical and chemical aspects of the interaction of laser radiation with matter.

Hererostructures of laser-sprayed cadmium sulfide on black silicon [7, 17] and copper sulfide also on black silicon [7, 18] were analyzed. Black silicon itself was obtained by physical and chemical methods. It is shown that the sputtering profile of these materials resembles the profile of black silicon. The problem of formation of laser-induced support centers in indium antimonite is considered [4, 25, 33]. Based on the two-dimensional lattice of sphalerite for indium antimonide, a cascade model of the excitation of the corresponding number and type of chemical bonds was constructed, which satisfactorily explains the observed results. In addition, based on this, a model is proposed that explains the influence of reirradiation and reabsorption processes on the distribution of donor centers in indium antimonide and on the shape of their distribution profiles [1-4, 33].

The formation processes of laser-induced urchin-type surface structures on silicon [12-14, 24] are also explained on the basis of a cascade model of excitation of the corresponding number of chemical bonds (coordination numbers) in the regime of saturation the excitation based on the phase diagram of silicon. It is shown that this process depends on the integral photon efficiency, and upon irradiation with nanosecond pulses of an excimer laser is more effective than when irradiated with femtosecond laser pulses from the near-infrared region of the spectrum.

Using the example of indium antimonide and indium arsenide, the influence of the spectral composition of optical radiation on the laser annealing of ion-implanted layers of these materials is shown [4].

The expediency of using laser radiation in lithography and production of black silicon and other similar structures is also shown [1-4, 7, 15, 16, 29-32].

Application of thin films using pulsed laser deposition

Typical simplified schematic diagram illustrating the pulse laser deposition is represented in Fig.1 [7].

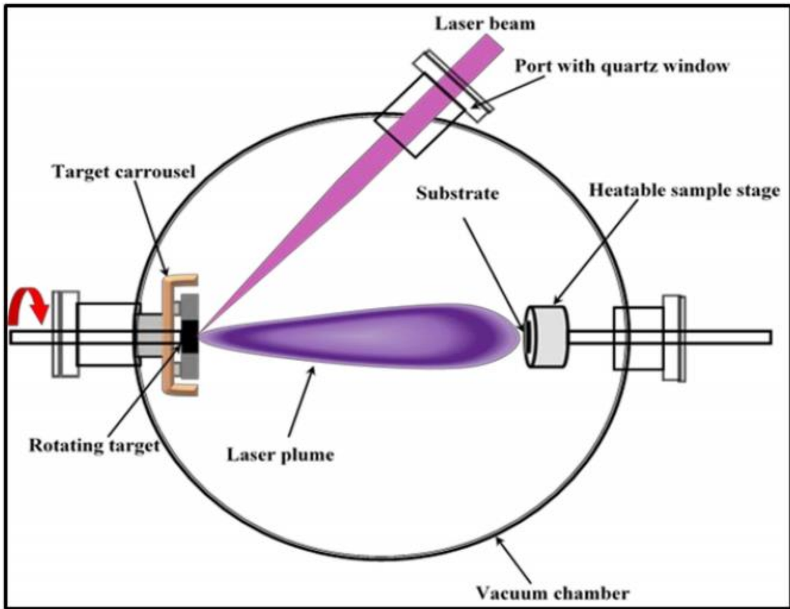

Fig 1: Simplified schematic diagram illustrating the pulse laser deposition [7]

Main three modes of of thin film growth are shown in Fig. 2 [2].

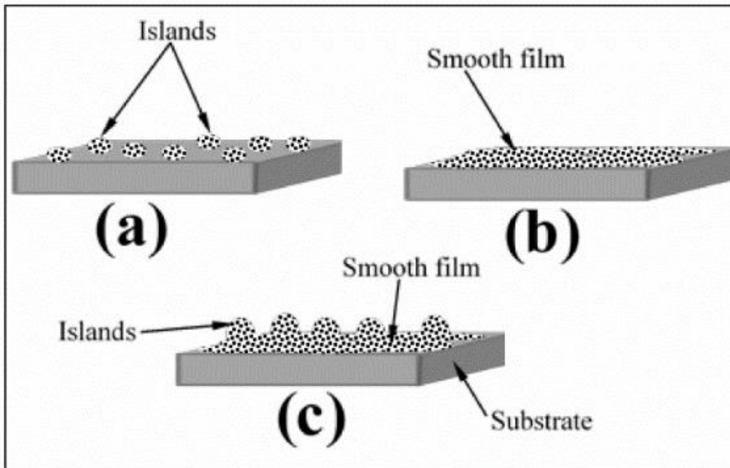

Fig 2: Modes of thin film growth: a) island; b) layer-by-layer; c) layer plus island [7]

Island or Volmer-Weber mode [3, 7]: an island growth occurs when the cohesion between the atoms of the target material is greatewr than the adhesion between the target atoms and the substrate. SAs a result, tha adatoms (atoms deposited on the surface of the substrate) are more bound to each other

that to the substrate, hence forming clusters. This mode of growth is characterized by three-dimensional islands (Fig. 2 a).

Layer-by-layer or the Frank - van der Merwe mode [3, 7]: layer-by-layer growth occurs when the adhesion between the adatoms and the substrate is greater than the cohesion between the atoms. This mode of grwth generally results in two-dimensional growth with the adatoms forming smooth monolayers on the surface of the substrate (Fig. 2 b).

Layer plus island or the Stranski-Krastanov mode [3, 7]: layer plus island growth mode occurs when islands are formed after the formation of one or two monolayers on the surface of the substrate (Fig. 2 c).

It should be noted that, in addition to thermodynamic models of nucleation and crystallization, electrodynamic models [3] can also be used (the phason model of V. Stafeev and the cascade model of the excitation of the corresponding number and types of chemical bonds in the excitation saturation mode). or from the solid state by sublimation.

Structure and morphology of thin films depoopsitrd using pulsed laser deposition is represented in Fig.3. The field emission scanning electron microscope (FESEM) cross-section image of the bSi fabeicated on Si substrate reported by Sarkar et al. [7, 18] is shown in Fig. 3a. The FESEM micrograph revealrd that the bSi vertical cone-shaped nanostructures of the diameter betwrrn 500 and 700 nm, height between 1 and 3 µm and tips of a few nanometers in diameter. The trabsmission electron microscope (TEM, Fig 3b [7, 18]) of the cross-section of the Si nanostructure revealed the nanocones shape. The porous structure of Si nanocones at the surface of nanocone resulting from the chemical etching is shown in the insert of Fig. 3 b. The selective area electron diffraction (SAED) pattern (Fig. 3c [7, 18]) confirmed that the core of NANOCONEs were crystalline DESPIte the pORE (2-5 nm) observed at the outer shell. Thr cross-sectionof the FESEM image of cthr CdS thin film laser ablatedon a bSi nanocones is shown in Fig. 3d [7, 18]. The FESEM micrograph confirmed a uniform coverage of CdS thin film with thickness between 50 and 80 nmn on the surface of the bSi nanocones. The thickness of some thin films recently deposited usind pulse laser deposited is represented in Table 1 [7]. The uniformity of CdS layere on the surface of nanocones is further confirmed by the FESEM image shown in Fig. 3e. As shown in Fig. 3f, the SAED pattern on the CdS/bSi heterojunction shows the diffraction rings confirming the polycrystalline nature of th CdS thin film. The SARD pattern also revealed the (002), (110) and (112) planes of wurtzite CdS [7, 18].

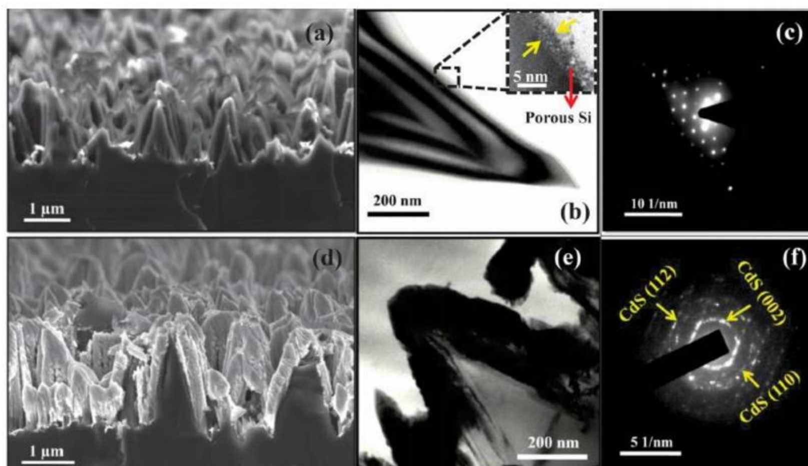

Fig 3: (a) Cross sectional FESEM image of Si nanocone arrays; (b) High-resolution TEM image of a single Si nanocone; (c) SARD pattern of Si nanocone; (d) Cross sectional FESEM image of CdS/bSi conical heterojunction arrays; (e) High-resolution TEM image of a single CdS/bSi nanocone conical heterojunction; (f) SARD pattern from the CdS/bSi nanocone heterostructure

The problem of formation a p-CuS-n-Si nanocone heterojunction based highly sensitive broad band photodetector is discussed in [7, 17]. Cone-like one dimensional Si nanostructures formed by metal (Au) assisted chemical etching, with superior antireflection characteristics have been used as templates for fabrication of the heterojunction. Covellite CuS material was synthesized by a simple chemical reaction for used as target material for the fabrication of p-CuS-n-Si nanocone heterojunctions via pulsed laser irradiation). p-CuS-n-Si radial heterojunction was fabricated by depositing a CuS layer on Au assisted etched Si nanostructures using KrF pulsed laser (l = 248 nm) ablation (2000 shots at a shot frequency 10 Hz) [7, 17]. Similar deposition was also carried out on bulk n-Si for use as the control sample. The distance between the target and substrate was kept fixed at 5 cm. By this method, a CuS film nearly 150 nm thick was deposited on nanotextured and planar n-Si. Finally to complete the device fabrication, a nearly 200 nm thick transparent and conducting Al doped ZnO (AZO) layer was deposited by the same PLD technique on both p-CuS/nanostructured n-Si and p-CuS/planar n-Si, which are hereafter referred to as the cone-like radial heterojunction device and control device, respectively.

Fig. 4(a) [7, 17] shows the cross-sectional field emission scanning electron microscopy (FESEM) image of the fabricated nano- structures on an n-Si wafer. Highly dense, vertically oriented cone-like nanostructures with

different heights and bases are observed. From the high resolution FESEM and TEM image of a single Si nanocone shown in Fig. 4(b) and (c) respectively, it is clear that the surface of the Si cones is porous in nature. Typical dimensions of the nanocone bases are 500-800 nm with the sharp tips having a diameter of a few nm. The heights of the nanocones are observed to be in the range of 2-4 mm. Fig. 4(d) [7, 17] shows the cross-sectional FESEM image of the CuS film deposited on the Si nanocones via pulsed laser deposition. The micrograph indicates conformal coverage of the CuS film on the Si nanocones. However, the bunching of several nanocones is clearly observed. The cross-sectional TEM image of a single Si nanocone coated with CuS (shown in Fig. 4e) [7, 17] again indicates the conformal surface coverage of nanocrystalline CuS over Si nanocones. A closer look at the Si-CuS interface of the nanocone textured Si indicates the formation of a rough interface due to the porous nature of the Si nanocone surface.

In the case of using chemical methods, it is necessary to form a certain concentration of crystallization centers on the surface, which lead to the appearance of "forests" of nanostructures.

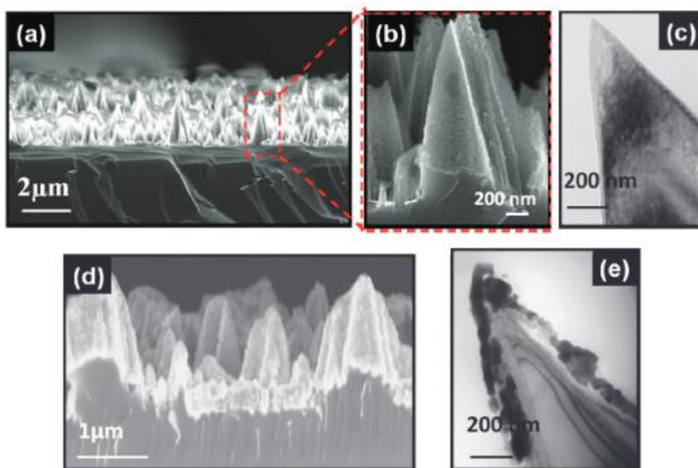

Fig 4: (a) Cross sectional FESEM image cone-like nanostructures on an n-Si wafer; (b) High-resolution TEM image of a single Si nanocone; (c) TEM image of Si nanocone; (d) Cross sectional FESEM image of CuS-nSi nanocone heterojunction; (e) Cross-sectional TEM image of a single CuS-nSi nanocone heterojunction; (f) Cross-sectional TEM image of a single Si coated with CuS [Kat]

Black silicon is called surface nanostructured silicon [19]. It was named so in 1999, and it was obtained during irradiation with pulses of a femtosecond laser [19]. Although it can be obtained by chemical and other methods. The

mechanisms of formation of laser-induced structures will be discussed in the next section of this work.

Results of other cases of laser deposite thin films are represented in Table 1 [7].

Table 1. Film thickness, laser poarameters and other variable parameters if pulse laser deposite thin films [7].

Material	Substrate	Laser/ laser prameters	Deposition time	Deposition atmosphere	Sybstrate Temperature (°C)	Thickness (nm)
CdS/p ±bSi	Si(110)	-	-	-	-	50 - 80
ZnO/MgZnO	saphire	Nd: YAG, λ=532, RR=10, LF = 1 - 2, PW=8	-	-	800. 700, 650	8, 5, 100, 450
Cu_2ZnSnS_4	Si	Nd: YAG, λ=355, RR=10, LF = 0.5-4, PW =4.7	45	-	300	50
ITO, AZO	PET	KrF excimer λ=248, RR=2, LF = 400, PW = 30	-	-	25, 125	100, 200
ZnO:Cu	Si	KrF excimer λ=248, RR=10, LF = 0.8, PW = 30	-	vacuum	-	40, 300
ZnO:Zn	Si(100)	Nd:YAG, λ=266, RR=10, LF = 40	25	Vacuum, Ar, O_2	300	80, 150, 285
ZnO:Zn	Si(100)	Nd:YAG, λ=266, RR=10, LF = 0.8, PW = 8	25	O_2	50, 200, 400	246, 414, 326
In_2Se_3	Transparent polyimide	KrF excimer λ=248, RR=4, LF = 100, PW = 20	12.5	O_2	300	22.9
Ca_2O_3	Si(100)	Nd:YAG, λ=266, RR=50, LF = 40	15	Vacuum, Ar, O_2	50 - 600	150
$ZnO:Tb^{3+}$	Si(100)	Nd:YAG, λ=266, LF = 40	15-55	O_2	300	150-500

$Y_3(Al, Ga)_5O_{12}:Ce^{3+}$	Si(100)	Nd:YAG, λ=266, RR=10, LF = 0.8	-	Vacuum, Ar	300	120, 270
$\beta-(Al_xGa_{1-x})_2O_3$	$\beta-Ga_2O_3$ (010)	KrF excimer λ=248, RR=10, LF = 0.3	-	O_2	800	70, 79
$\beta-Ga_2O_3$	Saphire	KrF excimer λ=248, RR=3, LF = 2	-	O_2	650	250, 350, 500
Ga_2O_3Sn	Saphire	KrF excimer λ=248, RR=3, LF = 2	-	O_2	650	112, 445, 510, 570
CaS	Si(100)	Nd:YAG, λ=266, 355, 512; RR=10, LF = 5.09, LE = 40	-	Ar	400	150, 162, 23

Remark to Table 1. λ = wavelength (nm); RR = repetition rate (Hz); LF = laser fluence (J/cm^2); RW = pulse width (ns); LE = laser energy (mJ)

Laser implantation as method of receiving of thin films

Let us now consider the modifications of laser-alloyed media without any additional processing. In the future, we will call such processes laser implantation [1 - 4].

First, let's consider the processes of formation of laser-induced donor-type layers on indium antimonide (Fig. 5 and Fig. 6).

The profiles of a distribution of volume concentration of n-centers N_v in p-InSb after laser irradiation are represented in Fig. 5 [25].

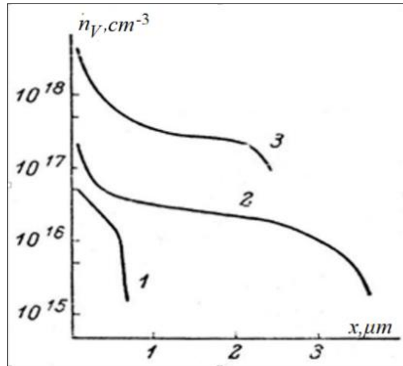

Fig 5: Profiles of the volume distribution electrons after laser irradiation of p-InSb. 1, 2-Ruby laser; 3-YAG:Nd laser. Energy density in pulse, J/cm^2: 1-5; 2 - 40 [25]

Regimes of irradiation were next: one pulse Ruby laser (wavelength 0.6943 μm, pulse duration 5 ms. curves 2, 3 of Fig. 5), multipulse Neodymium laser (wavelength 1.064 μm, pulse duration 10 ns, pulse rate 1 kHz, curve 1 of Fig. 5) [25].

The profiles of the distribution the photostimulated n-centers in subsurface layers p-InSb are represented in Fig. 6 [1, 4, 33]. Simple results were received for InAs too [1].

The samples of p-type conductivity are irradiated by one pulses Ruby laser (wavelength 0.6943 μm, pulse duration 20 ns) [1, 4, 33]. For intensity of irradiation $I_0 > 0{,}01$ J·cm^{-2} for InSb and $I_0 > 0{,}012$ J·cm^{-2} for p-InAs the n-layers on p-type materials are created [1, 4].

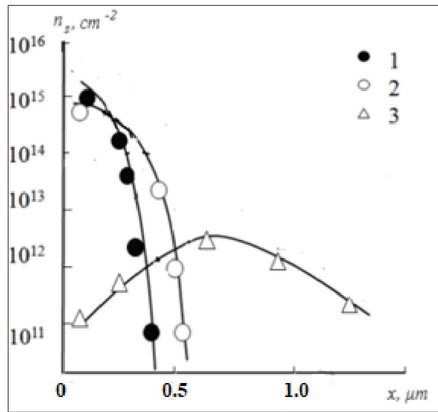

Fig 6: The profiles of distribution the layer concentration of the n-centers in p-InSb after ruby laser irradiation with various density of energy in pulse, J/cm^2: 0,07 (1); 0,1 (2); 0,16 (3) [1, 4, 33]

For intensity of irradiation $I_0 < 0,1$ J·cm^{-2} for InSb the profiles of the distribution of donor centers are represented the Buger-Lambert law (law of absorption the light in homogeneous media) [1, 4, 33]. For further increasing the irradiated intensity, the profiles of the concentration donor centers have diffusion nature. Further increasing of intensity of irradiatiuon are caused the visible destruction of irradiated matter (I_0>0,3 J·cm^{-2} for InSb). This effect has oriental character [1, 4, 33]. For crystallographic direction {111} the process of the creation damages is more effective as for direction {110} [1, 4].

Laser-induced generation surface nano and microstructures in Ge and Si may be represent as laser-implantation phenomena too [4].

Detail research of creation the surface laser-induced structures for silicon, germanium and other semiconductors are represented by A. Medvid' in [28]. Samples of Ge {111} and Ge {001} i-type single crystals are used in experiment. Nd: YAG laser (wavelength 1,064 µm, duration of pulse 15 ns, pulse rate 12,5 Hz, power P=1 MW) was used for the irradiation.

The AFM picture of Ge surface after Nd laser irradiation is represented in [28]. Laser-induced Ge nanohills have hexagonal structure and height to 200 nm [28].

More detail investigation of morphology the creation of surface laser-induced structures of Si was made in [12-14]. The typical microcolumn morphology of silicon, which are irradiated by pulse eximer laser radiation (pulse duration 25 ns, wavelength 248 nm) SF_6 atmosphere is represented in Fig. 7 [12-14].

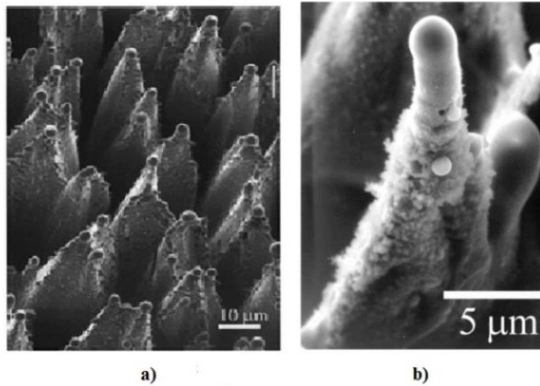

Fig 7: a) Walled Si structure produced by 2040 laser pulses at E_d =1.5 J/cm^2 in 1 atm of SF_6 [12, 13]; b) Si specimen laser-irradiated at 3.2 J/cm^2, first with 7500 pulses in a 0.25 bar ambient pressure of SF_6 and subsequently with 500 additional pulses in an ambient pressure of 0.2 bar O_2 + 0.8 bar N_2 [14]

Similar urchin-like structures were obtained by irradiating silicon crystals with femtosecond laser pulses (pulse duration 130 fs, irradiation wavelength 800 nm, number of pulses 400) [24]. However, the first regimes of irradiation [12 - 14] had a higher photon efficiency per pulse [1, 2].

These experimental results indicate that the urchin-like structure is caused by phase transitions of structures with initial cubic symmetry into structures with less order of symmetry (hexagonal, triclinic, etc.) and that radiation absorption conditions play a major role in this [1, 2].

Generation of surface and subsurface cascade laser-induyced optical breakdoiwn in SiC [21, 22] and KCl [22], roughly speaking, are processes of laser nimplantation.

Volume experimental data we are showing on the example of silicon carbide [21, 22] (Fig. 8).

Experimental data, which allow to see microscopic structure of optical breakdown, are representing in Fig. 8. Sectional area of receiving structures was ~ 22 µm, the depth of ~ 50 µm. As seen from Fig. 8 (c) we have five stages disordered regions, which are located at a distance from 2 to 4 µm apart vertically [21, 22]. Branches themselves in this case have a thickness from 150 to 300 nm. In this case there are lines in the irradiated nanocavity with spherical diameter of from 15 nm to 20 nm (Fig. 6). In this case, irradiated structures have crystallographic symmetry of the initial structure. We see that this process have cascade nature and only last stage of this cascade are represented "clean" breakdown (Fig. 8).

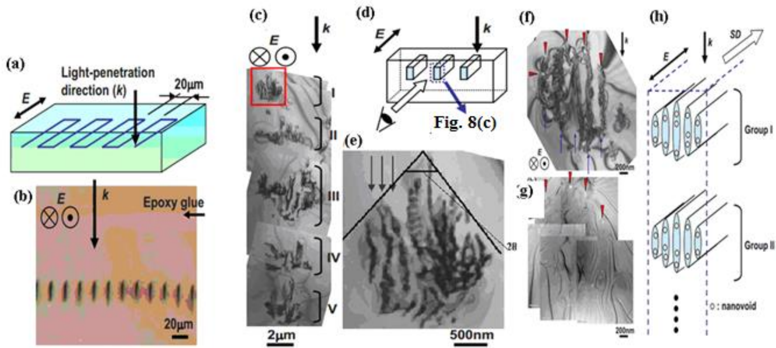

Fig 8: (a) Schematic illustration of the laser irradiated pattern. The light propagation direction (k) and electric field (E) are shown. (b) Optical micrograph of the mechanically thinned sample to show cross sections of laser-irradiated lines (200 nJ/pulse). (c) Bright-field TEM image of the cross section of a line written with pulse energy of 300 nJ/pulse. (d) Schematic illustration of a geometric relationship between the irradiated line and the cross-sectional micrograph. (e) Magnified image of a rectangular area in (c). Laser-modified layers with a spacing of 150 nm are indicated by arrows. (f) Bright-field TEM image of a portion of the cross section of a line written with a pulse energy of 200 nJ/pulse. (g) Zero-loss image of a same area as in (f) with nanovoids appearing as bright areas. Correspondence with (f) is found by noting the arrowheads in both micrographs. (h) Schematic illustrations of the microstructure of a laser modified line. Light-propagation direction (k), electric field (E), and scan direction (SD) are shown. Only two groups (groups I and II) of the laser-modified microstructure are drawn [21, 22].

Two parallel channels of optical laser-induced breakdown were obtained for potassium chloride when it was irradiated with nanosecond CO_2 laser pulses (pulse duration 30 ns, irradiation energy 2 J/cm^2, TEM_{01} irradiation mode) [20].

A significant difference from the results of Fig. 8 and that the distance between the cascade groups for silicon carbide is 2-3 μm (Fig. 8), while for potassium chloride it is 30-40 μm [20]. The microscopic nature of the fractures was not obtaining for potassium chloride, as photography[20] (resolution 1.5 - 2 μm) was using to obtain the picture, while electron microscopy [21, 22] (resolution 2-3 nm) was used for silicon carbide. This is what made it possible to observe the generation of nanovoids with sizes of 15-20 nm (Fig. 8 (f) - (h)).

Main peculiarities of represented experimental data is showing its complexity. Roughly speaking we have trace of resulting interaction light and matter in irradiated matter.

In contrast to Nonlinear Optics, where we study the processes of interaction of light with matter as a change in radiation characteristics, in relaxation optics we study the processes of phase transformations of irradiated matter. It is obvious that we should investigate this problem from a physical-chemical point of view. Thus, classical, non-linear optical effects are associated with mixed absorption. The concentration of absorption centers in this case ranges from 10^{14} to 10^{17} cm^{-3}. Phase transformations of the irradiated material are due to changes in the structure of the irradiated material, that is, concentrations 10^{22} cm^{-3} [1 - 4]. Therefore, we must search new methods of modeling.

Thus, the use of physical-chemical methods to evaluate the energetic characteristics of non-linear optical phenomena makes it possible to develop a universal approach for their evaluation. For an example, let's take the definition of the threshold for the formation of self-focusing. The well-known formulas of Kelly and Marburger allow us to give these estimates only for Kerr media, which roughly speaking is liquids and some solids [2]. Physical-chemical evaluations give the same values as the Kelly and Marburger formulas. In this case, we are only interested in the concentration of the corresponding light absorption (scattering) centers. In addition, such an approach makes it possible to evaluate the chain of processes that lead to the observed phenomena from a single point of view [1 - 3].

Now we show the using of cascade model for the explanation experimental data of laser-induced surface physical-chemical phase transformations in silicon (Fig. 7 [12 -14]) and germanium [28].

The rough estimation of the energy characteristics of corresponding processes may be represent with help formula (1).

$$E_{ir} = \sum_i N_i \hbar\omega_i, \qquad (1)$$

where N_i is the concentration of proper centers of light scattering, $\hbar\omega_i$ is photon energy, ħ is Planck (Dirac) constant [1 - 4].

For self-absorption the number of the scattering centers N_i is equal the atom density the lattice N_a, which can be determined with help of next formula [1 - 4]

$$N_a = \rho \frac{N_A}{A}. \qquad (2)$$

Where N_A – Avogadro number, ρ – density of semiconductor, A-a weight of one gram-atom or gram-molecule.

For indium antimonite $N_a \sim 4 \cdot 10^{21} cm^{-3}$. For more detail estimation of the results of Fig. 1 and Fig. 2 we are used the two-dimensional lattice (Fig.9) [1, 4, 33].

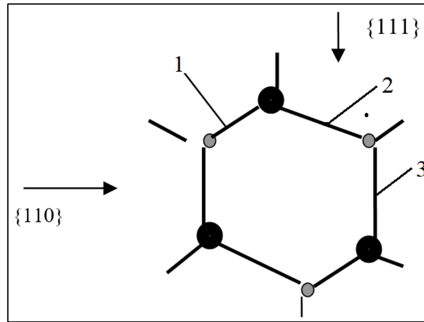

Fig 9: Two-dimensional picture the crystal lattice A_3B_5 (including InSb and InAs) the cubic symmetry (sphalerite). Bond 1 is pure covalent has energy 0.18 eV, bond 2 - 1.95 eV, bond 3-2.15 eV [1, 4, 33]

Main estimations may be made with help modified formula (1)

$$E_{ir} = \sum_i N_a \varepsilon_{bi}. \qquad (1a)$$

Where ε_{bi} is the energy of proper bonds from Fig. 9 (I =1, 2, 3).

The breaking of bond 1 in the regime of saturation of excitation is corresponds to laser effect with optical pumping [1, 4, 33]. This effect has large differential photon efficiency, which can be determined with help formula (3)

$$n = 2ln\frac{\hbar\omega_r}{E_g}, \qquad (3)$$

Where $\hbar\omega_r = 1.78\, eV$ for Ruby laser radiation, $E_g = 0.18\, eV$ and equaled of energy of bond 1. Crystals of indium antimonite in the sphalerite modification are direct-band, so the band gap corresponds to the minimum chemical bond energy. For InSb n = 4.8. This fact is caused te increasing of relaxation time ~ 10^{-7} s for Ruby laser irradiation[1, 4, 33].

These data were using for the estimations of laser-induced damages (Rurherford backscattering spectra of protons with energy 500 keV) in InSb after Ruby-laser irradiation [4]. Maximal value of Rutherford defectiveness is corresponding to value 0.1 J/cm^2. This value is correlating with curves 1 and 2 of Fig. 6 and corresponds to the breaking of bonds 1 and 2 in Fig. 9 [4, 33].

At the same time, one connection is the seed for other connections. Only in the mode of saturation of excitation of the previous connection (connections) do we have minimal energy expenditure to obtain the desired result (curves 1 and 2 of Fig. 6).

Schema of Fig. 9 was using for the explanation the oriental effect of creation laser-induced n-centers in InSb. The angle between directions {111} and {110} is equal 37,5° for the bond 1. Therefore, coefficient of the anisotropy the the creation laser-induced centers is equal the square of the tangent of this angle-0,45. Effective cross-section of absorption in {111} is more intensive as in direction {110} [4].

The rupture of all three bonds leads to the appearance of a diffusion profile (curve 3, Fig. 2). The estimates made according to formula (1a) confirm our reasoning [4, 33].

Form of profiles Fig. 6 was explained using the photokinetic model (adapted model of the phytoeffect). At the same time, curves 1 and 2 Fig. 2 correspond to the kinetic approximation, and curve 3 Fig. 2-to dynamic (two-diffusion approximation) [4]. In the latter case, the difference in coefficients of laser-induced diffusion (self-diffusion) of indium and antimony atoms is assumed [4].

To estimate the life time of the corresponding processes, a phenomenological chain of relaxation times was constructed, which allows us to explain non-equilibrium and irreversible laser-induced processes from a single point of view [4, 33].

The experimental results of Fig. 5 [25] can be explained in a similar way. Curve 1 of Fig. 5 has the same form as curves 1 and 2 of Fig. 6.

But the integral efficiency of transforming radiation into irreversible changes for the data Fig. 6 is larger by 2-3 orders of magnitude, as for Fig. 5. This is explained by the fact that in the latter case, reradiation processes with photon energy of 0.18 eV play a major role. This is confirmed by the results of curves 2 and 3 of Fig. 5. The shape of the profiles of these curves in the upper region corresponds to the absorption coefficient with a coefficient of $2{\cdot}10^5 cm^{-1}$ for Ruby laser irradiation and 10^5 cm^{-1} for neodymium laser, the tail parts correspond to an absorption coefficient of the order of 100 cm^{-1} of reradiation with a photon energy of 0.18 eV [4].

This means that a large contribution to the shapes of profiles 2 and 3 Fig. 5 give the processes of reirradiation and reabsorption. The number of acts of reradiation can be estimated using formula (4) [1].

$$n = \frac{\tau_i I_{sat}}{\tau_r\left(1-\frac{\tau_r}{\tau_i}\right)I_0} \tag{4}$$

Where τ_i is time of irradiation, τ_r is relaxation time, I_{sat} - the intensity of saturation of excitation (curve 2 of Fig. 6) and I_0 - the intensity of irradiation.

After substitution proper value of I_{sat} and I_0 from Fig. 5 and Fig. 6 we have n $\cong 10 \div 500$.

Experimental data of Fig. 1 are certificated this hypothesis. Surface and volume concentrations donor centers in InSb after irradiation of nanosecond Ruby-laser pulses (curves 1 and 2 of Fig. 6) is more in 3-4 orders as after millisecond irradiation (curve 2 of Fig. 5). For this case we are using next model. The part of absorbed irradiation with including process of n-reirradiation may be represented as

$$I_n = \frac{\frac{\tau_r}{\tau_i}}{1+\frac{\tau_r}{\tau_i}} I_0 e^{-\alpha x}. \quad (5)$$

For this case we have $\frac{\tau_r}{\tau_i} = 0.05 - 0.1$. For Ruby laser irradiation (curve 2 of Fig. 1) we can determine relaxation time $\tau_r = (0.05 - 0.1)\tau_i = (0.25 - 0.5)ms$.

For estimation the efficiency of generation n-centers for the nanosecond (curve 2 of Fig. 6) and millisecond (curve 2 of Fig. 5) regimes of irradiation we used next formula.

$$\beta = \frac{I_{sat}/N_{avsat}}{I_{ir}/N_{avir}}. \quad (6)$$

This formula give next values: $2.5 \cdot 10^{-6}$ for subsurface part of curve 2 of Fig. 5 and $2.5 \cdot 10^{-7}$ for tail part of curve 2 of Fig. 5. For curve 1 of Fig. 5 this efficiency is equaled $2 \cdot 10^{-6}$. Therefore, processes of reirradiation may be used for the formation more deep parts of irradiated matter [2, 4].

Thus, the model based on Fig. 9 makes it possible to explain the main regularities of changes in electrophysical characteristics of irradiated antimonide and indium arsenide, but does not allow evaluating laser-induced structural changes.

However, it is possible to build a model that allows you to estimate laser-induced structural changes in irradiated materials. Thus, to explain the experimental results Fig. 7, a physical-chemical model was built based on the phase diagram of silicon (Fig. 10) [26].

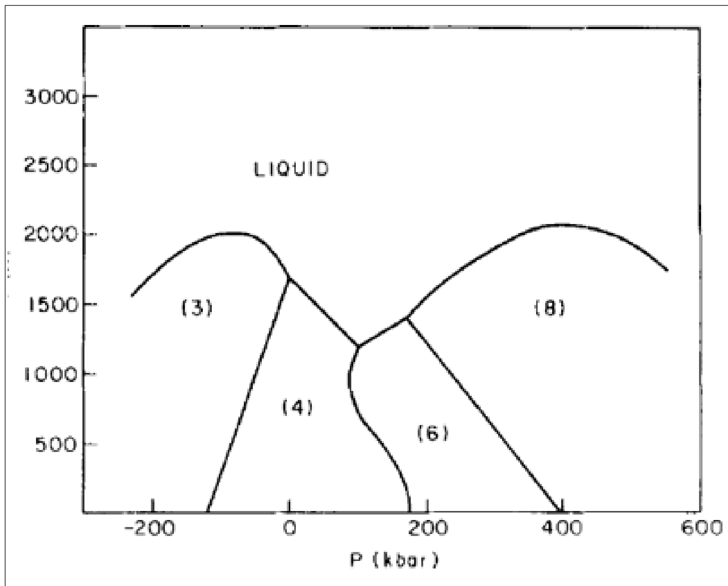

Fig 10: A schematic phase diagram for Si(CN). The coordination numbers (CN) of the various phases are indicated. The diagram is based on common features of the phase diagrams of column IV elements as described by the references cited in Pistorius's review [18]

Starting from a high temperature >$3 \cdot 10^3$K and subject to a constraint of average density $\langle\rho\rangle = \rho(4)$, a hot micronucleus will tend to bifurcate into the most stable phases (highest T_m) which straddle Si(4) in density. These are Si(3) and Si(8), as indicated by the diagram [26].

It can be seen from this figure that silicon (by analogy with germanium) has four crystallographic modifications, and taking into account quasi-crystalline modifications-twelve [1]. We will dwell only on crystallographic modifications.

To determine the energy that falls on one coordination or layer, we will use the Seitz energy definition from the radiation physics of a solid body [1]. This energy of the silicon is equal to 12.6 eV, and the number of nearest neighbors is equal to the coordination number. In addition, in the diamond lattice, all bonds are covalent and equal to each other. We know that one coordination number in silicon corresponds to an energy of 1.6 eV. For germanium-1.3 eV for similar reasons. By the way, this energy is equal to the energy of the corresponding covalent bonds by L. Pauling [1]. Next, if we multiply the value of this energy by the density of atoms of the corresponding lattice and by the difference in the corresponding coordination numbers, we

will obtain the corresponding value of the transition energy from one crystallographic modification to another.

These considerations are the basis of the cascade model of step-by-step excitation of proper chemical bonds in the regime of saturation the excitation were used [1 - 4]. This model in based on the phase diagram of of Fig. 10 [26].

Let initial crystal semiconductors Si and Ge have, the diamond structure.

We have from formula (2) for Si $N_{aSi} = 5 \cdot 10^{22} cm^{-3}$, and for Ge $N_{aGe} = 4.4 \cdot 10^{22} cm^{-3}$. Please, leave two blank lines between successive sections as here. However, Si and Ge may be crystallizing in lattices with hexagonal, cubic, trigonal and monoclinic symmetry [1 - 4].

Coordination number (CN) 8 is corresponded of diamond lattice, CN 6 - hexagonal lattice, (CN) 4 and (CN) 3 - other two lattices. It should be noted that melting temperatures of these phases are various. Volume density of CN is equaled $CN \cdot N_a$. For diamond symmetry of lattice, this value is $8N_a$ [1].

We can determine corresponding volume density of energy, which is necessary for transition between proper crystal structures with help formula (1a).These data are represented in Table 1.

Table 2: Volume density of energy I_{vi} (10^3 J/cm^3), which is necessary for the breakage of proper coordination numbers (CN) in the regime of saturation of excitation in Si and Ge [1, 4]

Compound	I_{v1}	I_{v2}	I_{v4}	I_{v5}
Si	12.8	25.6	51.2	64
Ge	7.6	15.1	30.2	37.8

To obtain the surface density of irradiation energy, we must divide the value given in Table 2 by the corresponding light absorption index. These results are analyzing in [1, 4]. As in the case of indium antimonide, differential photon efficiency (light absorption conditions) is crucial for silicon. This explains why the efficiency of formation of microstructures by nanosecond pulses of an excimer laser with a photon energy of 4.25 eV is greater than by femtosecond laser pulses with an energy of 1.51 eV [1]. Concept of photon efficiency [2] is generalizing of concept photochemical efficiency [2].

Roughly speaking, the efficiency of the formation of microcolumns for irradiation with an excimer laser is determined by the processes of splitting the photon energy, as it can be spent on breaking more than two chemical bonds, while the energy of a photon with an energy of 1.51 eV is not enough to break one bond for silicon. In the latter case, we must implement the multiphoton absorption mode. The same zone of photochemical reactions is

determined by the absorption coefficient of laser radiation. For excimer laser irradiation, it will be one and a half orders of magnitude smaller than for longer-wavelength irradiation.

Let us now turn to the explanation of the experimental results of the optical analysis of silicon carbide [21, 22] and potassium chloride [20].

The first explanations were based on the heterogeneity of the irradiated material, which led to a plasma or thermal breakdown. This is explained by the fact that the experimental results for potassium chloride did not allow us to see the cascade of processes that lead to the actual optical breakdown. In fact, laser-induced optical breakdown is a concentration of energy with a Seitz energy density [1 - 4], and we have no choice but to find ways to realize this concentration.

That is why a cascade model was proposed, which is based on the transformation of the initial exposure and the creation of non-uniform exposure of the material [3]. This cascade is including diffraction stratification of focused radiation, generation of conical Cherenkov radiation, interference of the short-wavelength part of Cherenkov radiation, and actual optical breakdown in the maxima of this interferogram [3].

Diffraction stratification and generation of surface Cherenkov radiation belong to the first group (Fig. 8). The second group includes optical breakdown, including the formation of nanovoids (Fig. 6).

Diffraction stratification was modeling with help of Rayleygh rings concept [3].

Cherenkov radiation may be certified with macroscopic [23] and microscopic [34] ways.

The Golub macroscopic [23] and A. Bohr [34] microscopic mechanisms were synthesizing with help of next formula [3].

$$\theta_{ch} + \alpha_{ir} = \pi/2 \text{ or } \theta_{ch} = \pi/2 - \alpha_{ir}, \qquad (7)$$

Where θ_{ch} – Cherenkov angle, α_{ir} – angle between tangent line and direction of laser beam.

Angle α_{ir} was determined from next formula [1], [4]

$$tan\alpha_{ir} = d_b/l_f, \qquad (8)$$

where d_b - diameter of laser beam, (7 mm), l_f - length of focusing or self-focusing. In our case α_{ir} is angle of focusing or self-focusing.

This formula is approximate for average angle α_{ir} for proper foci. The Golub formula (8 a)

$$cos\theta_{Ch}=\frac{c}{n_2(\omega)v_{nlpol}}, \quad (8\ a)$$

Was using for the determination of corresponding order of diffraction ring may be determined with help next formula [3]

$$l_{nf} = \frac{d_{ndif}}{2tan^{\varphi}/_2}. \quad (9)$$

According to Fig. 8 (c) we have five diffraction rings. Each surface of cone this diffraction stratification is source of Cherenkov radiation. This is confirmed by experimental facts that supercontinuum (Cherenkov) radiation has a surface character [3].

The estimation of energy distribution in five Mach cones was made by next formula [1], [4]

$$E_{1ob} = \frac{\pi^2}{4}\left(\sum_{i=1}^{5} n_{iav}^2\, l_{iav}\right) r^2 N_{asiC} E_{Zth}, \quad (10)$$

Where n_{iav}-average visible number of filaments in proper group of cascade, l_{iav}=1000 nm-average length of filaments in proper group of cascade, r = 10 nm - average radius of filament, N_a - atom density of 4H-SiC [3].

The atom density of 4H-SiC may be determined with help formula (2). For 4H-SiC $N_{aSiC} = 9.4 \cdot 10^{21} cm^{-3}$.

Energy, which is necessary for the optical breakdown our nanotubes may be determined in next way. Zeitz threshold energy for 4H-SiC is equaled E_{Zth} ~ 25 eV [3]. Let this value is corresponded to energy of optical breakdown. Therefore, summary energy E_{1ob} is equaled

$$E_{1ob} = N_{asnt} \cdot E_{Zth} = 23.2\ nJ. \quad (11)$$

This value is equaled of ~ 8% from pulse energy or ~ 30% from the effective absorbed energy of pulse [3]. As we can see, Cherenkov radiation generates laser radiation more effectively than charged particles or gamma radiation.

If this scenario is true, we have as for 4H-SiC effective transformation the energy of laser radiation to cascade of laser-induced breakdown for KCl too. This value is 11,6 - 17,4 percents [3].

The sizes of nanovoids (Fig. 8 (h)) may be determined with help modified Rayleygh model [3] and its form-the help methods of continuum mechanics [3] in next way.

For the estimations of maximal radius of nanovoids we must use modified Rayleygh formula [3]

$$R_{max} = \frac{2R}{0.915r}\sqrt{\frac{E_{ir}}{\pi\tau_{ir}cE}}, \quad (12)$$

where T_c-the time of creation the nanovoid (bubble), R is radius of nanovoid, r-radius of irradiated zone, E - Young module, E_{ir}- energy of one pulse. τ_{ir}-duration of pulse [3].

If we substitute r = 250 nm, R = 10 nm, E = 600 GPa [3], E_{ir}=300 nJ, τ_{ir} = 130 ps, $c=3\cdot10^8$ m/s, than have R_{max}=11 nm.

The velocity of shock waves for femtosecond regime of irradiation is less as velocity of sound. However, we have two velocities of sound in elastic body: longitudinal v_{ls} and transversal v_{ts} [3]. Its values are determined with next formulas

$$v_{ls} = \sqrt{\frac{E(1-\nu)}{\rho_0(1+\nu)(1-2\nu)}}, \text{ and } v_{ts} = \sqrt{\frac{E}{\rho_0(1+\nu)}} \quad (13)$$

Where ν-Poisson's ratio [3]. The ratio between of these two speeds is equaled.

$$\alpha = \frac{v_{ts}}{v_{ls}} = \sqrt{\frac{(1-2\nu)}{2(1-\nu)}}. \quad (14)$$

However, this ratio must be true for shock waves too. Therefore, for silicon carbide for ν = 0,45 [3] α = 0,33. Roughly speaking last ratio is determined the step of ellipsoidal forms of our nanovoids (Fig. 8 (h)).

In this case, we represented 4H-SiC as isotropic plastic body. For real picture, we must represent hexagonal structure. However, for the qualitative explanation of experimental data of Fig. 8 (h) this modified Rayleygh model allow explaining and estimating the sizes and forms of receiving nanovoids [3].

We can estimate sizes and forms of possible nanovoids for potassium chloride too. Let's take the ratio of the radius of the irradiation zone to the radius of the nanowire as 50. The energy of irradiation is 2 J. The duration of irradiation is 50 ns. Young's modulus 29.67 GPa, Poisson's ratio 0.216 [3].

After substitution, these data to formula (14) we have $R_{maxKCl} = 62.5nm.$ Ellipticity of KCl nanovoids may be determined from (14) $\alpha_{KCl} = 0.6$.

Let us now estimate the maximum bubble radii for the acoustic case. For this, in formula (12), you need to change the speed of light to the speed of sound (12 a).

$$R_{max}^{ac} = \frac{2R}{0.915r}\sqrt{\frac{E_{ir}}{\pi\tau_{ir}c_s E}}, \quad (12\ a)$$

Where c_s is speed of sound.

As a result, we get $R_{maxSiC}^{ac} = 1.7\mu m$ and $R_{maxKCl}^{ac} = 28\mu m$. The shape of the voids does not change, they just increase in size by 2-3 orders of magnitude [3].

If we take the ratio of the acoustic formula (12 a) and the optical formula (12), then for the same irradiation modes we have the ratio

$$\frac{R_{max}^{ac}}{R_{max}} = \sqrt{\frac{c}{c_s}}. \quad (15)$$

However, a comparison with the experimental results (Fig. 3) and [20] shows those electromagnetic rather than acoustic processes play the main role in the formation of nanovoids. This is explaining by the fact that in this case a chain of close-range coherent processes of transformation of both optical radiation into the excitation of the medium and the corresponding relaxation of the medium is implemented, in other words, there is a chain of interconnected coherent transformations.

Other complex treatments, including laser annealing of ion-implanted layers of semiconductor materials, photolithography, etc.

Let us now consider some more complex technological processes in which laser radiation is used.

The results of the positive resolution the problem of laser annealing of ion-implanted InSb and InAs are represented [4]. The conclusion of previous chapter may be next: the laser annealing of these semiconductors the Ruby and neodimium laser radiation is impossible. For more precision research of this hypothesis the Ruby laser and CO_2-laser irradiation the Mg^+/InSb, Mg^{++}/InSb and S^+/InAs were provided. The results of integral researches for InSb are represented in Fig. 11. Next types of the irradiation were used. Pulse Ruby laser regime had next parameters: pulse duration $\tau_i = 2 \cdot 10^{-8} s$; wavelength $\lambda = 0{,}6943\mu m$; density of energy flow $I_0 = (0.001 - 0.3)\ {}^{J}/{}_{cm^2}$. Pulse CO_2-laser - $\tau_i = 10^{-6} s$; wavelength $\lambda = 10{,}6\mu m$; density of energy flow $I_0 = (0.01 - 10)({}^{J}/{}_{cm^2}$. And stationary CO_2-laser - $\tau_i = (10^{-6} - 10)s$; wavelength $\lambda = 10{,}6\mu m$; density of power $W_0 = (10 - 30)\ {}^{W}/{}_{cm^2}$.

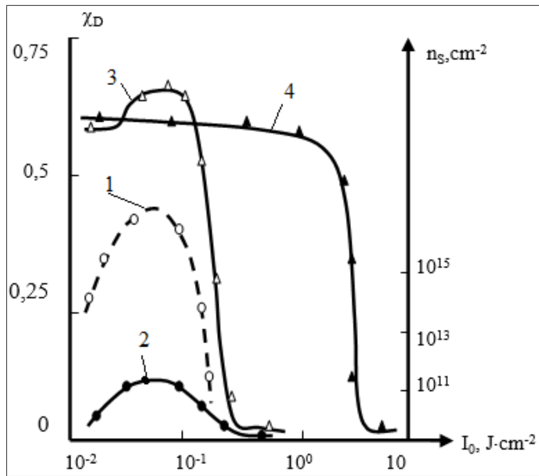

Fig 11: Laser effects in InSb and Mg^+/InSb [4]: 1-the energetic dependence of the creation the donor centers in InSb (points are experimental data); 2 - $\chi_D = f(I_0)$ in InSb; 3,4 - $\chi_D = f(I_0)$ in Mg^+/InSb after ruby laser (3) and CO_2-laser (4) irradiation

The curves 1, 2 and 3 in Fig. 11 are correlated. It is explained as fact of the addition optical damages to radiation defects for intensity of irradiation 0,04 ÷ 0,1 $J{\cdot}cm^{-2}$. Further increasing the intensity to provide to the interaction with optical and radiation damages, but in this case the more important role has heating phenomena. For more small intensity of the irradiation $\left(I_0 < 0.04\ ^{J}/_{cm^2}\right)$ the level of the defective state isn't increased. The comparative analysis these data with results of Fig. 6 show why laser annealing is impossible for Ruby laser irradiation. In this case the full activation the implanted admixture isn't existed for all possible regimes of the irradiation.

The application for laser annealing CO_2-laser ($E_a \leq h\nu \leq E_g$) [4, 33] the activation of implanted admixture was attained. The radiation defects are annealed for all regimes of the irradiation (stationary and impulsive). The result of the application the impulse CO_2-laser for annealing Mg^+/InSb are represented on curve 4 Fig. 11. The increasing of the level the defective state as for curve 3 is absented. The correlation between thresholds the melting and the heat destruction the InSb for Ruby-laser and CO_2-laser irradiation were 1:10 and 1:3 respectively. The explanation of this fact is next. For Ruby-laser ($h\nu > E_g$) process is provided on succession the creation of optical damages-heating, including reconstruction and annealing primary damages and creation secondary heating defects, -melting-destruction. For CO_2-laser this succession is more shortly: heating-melting-destruction. Coefficient of the creation

damages of two-photon absorption is small. In the case of laser annealing of ion-implanted layers the index of the absorption of ion-implanted layer is 10^4 cm^{-1} thus as for pure materials one is 10 cm^{-1}. For comparison, index of the own absorption for ruby laser is $2\cdot10^5 cm^{-1}$. Thus for CO_2-laser annealing the process has next succession photostimulated and thermal annealing. Both processes (quantum and temperature) have one direction. It are corresponded the independence this experimental data of time irradiation for this process. In our researches the processes of the melting after CO_2-laser irradiation are not observed. The electrophysical properties of laser annealed layers (Volt-Ampere characteristics) is shown the activation the implanted admixture. For increasing the intensity of the irradiation of stationary laser in 3-4 order than for annealing samples are heated to red color and sublimated. In general case the laser irradiation with $h\nu>E_g$ may be used for laser annealing for more long time of irradiation (~10^{-3} s and more). For any intensity of the irradiation process of the annealing may be more intensive than processes of the optical and temperature creation of the damages. For this time of the irradiation the concentration of the thermodefects, implanted admixture and optical defects may be correlated for various regimes of the irradiation.

The receiving the n-layers on *p*-I*nSb* and *p-InAs* after irradiation the pulse Ruby laser [4, 33] allow have these devices. But best p-n junctions were be receiving with help mixed ion-laser irradiation (ion implantation and CO_2-laser irradiation). Last structures have best characteristics than first. The problems of the creation various p-n junctions and its theoretical discussion are represented too.

The influence of spectral range of laser irradiation on the creation the irreversible changes in *InSb* and *InAs* were represented in [4]. The renewal structure and full activation of the impurity in Mg^+-implanted layers $InSb$ is possible only for the CO_2-laser irradiation with density of energy flow $I_0 = 10 J/cm^2$ [4]. This effect is integral and isn't depended from the regime of irradiation (pulse or stationary). The renewal of structure is happen after impulse Ruby irradiation with $I_0 = 0.1 J/cm^2$ in measurement Rutherford backscattering spectra ion H^+ with energy 500 keV (curve 2 of Fig. 11) and He^+ with energy 1,8 MeV (curves 3 and 4 of Fig. 11). But activation of the impurity isn't happen [4].

The relative changing of the crystal state was determined in surface layer with help relative defectiveness [32].

$$\chi_D = (H_{ir} - H_{ch}) / (H_r - H_{ch}), \quad (16)$$

Where H_{ir} and H_{ch}-the exit of backscattering ions for radiated and unradiated crystall in the channeling regime, H_r-the exit of backscattering ions for unradiated crystal in random regime. χ_D is calculated on depth more than depth of ion-implanted subsurface layer.

The renewal structure and full activation of the impurity in Mg^+-implanted layers $InSb$ (ion energy 100 keV, dose $6 \cdot 10^{14}$ cm^{-2}) is possible only for the CO_2-laser irradiation with density of energy flow $I_0 = 10 J/_{cm^2}$ [4]. Analogous process renewal structure and full activation of the impurity in S^+-implanted layers *InAs* (ion energy 40 keV, dose 10^{14} cm^{-2}) is possible for the CO_2-laser irradiation with density of energy flow $I_0 = 12 J/_{cm^2}$ [4].

However, the creation of new donor centers in InSb, InAs and Si after impulse laser irradiation with $h\nu < E_g$, where E_g - band gap of semiconductor, allow to receive n - p junctions. n-layers were stable for the $I_0 = 0.1 J/_{cm^2}$ for $InSb$ and $I_0 = 0.16 J/_{cm^2}$ for InAs. Corresponding Volt-Ampere characteristics are curve 2 (InSb) and curve 3 (InAs) on Fig. 12 [4]. These characteristics have more "bad" character as characteristics of curves 1 and 4.

This difference may be explained in the following way. The CO_2-laser annealed ion-implanted layers (LAIIL) are the more stable centers as Ruby laser induced donor layers (LIDL). The depth of LAIIL is 0,2-0,4 μm, the depth of LIDL-0,6-6 μm [4]. The edge of ion-implanted layer is more abrupt as laser-induced layers. It are basic causes of the best electrophysical properties LAIIL as LIDL.

The difference between physical properties of the LAIIL and LIDL supplement the explanation of the conclusion about impossibility of the laser annealing ion-implanted layers with irradiation in regime with $h\nu > E_g$ [4]. The index of absorption in pure $p - InSb$ of the CO_2-laser irradiation is $10 cm^{-1}$, Ruby laser - $2 \cdot 10^5$ cm^{-1}. The index of absorption in Mg^+/InSb layers of the CO_2-laser irradiation is $10^4 cm^{-1}$. Therefore, in the first regime (curve 1, Fig.6) of the irradiation we have one process-light scattering on metastable centers and this effect isn't depended from the time of the irradiation. The heat effects (for impulse regime of the irradiation) have the same direction as photoinduced phenomena.

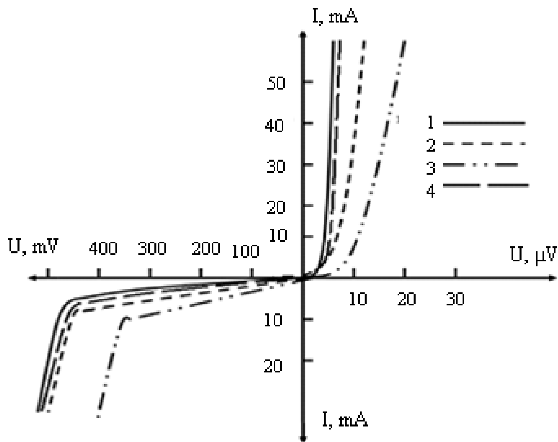

Fig 12: Volt-Ampere characteristics p-n and n-p junctions: LAIIL, curve 1 - Mg^+/InSb [4], curve 4 - S^+/InAs [4]; LIDL, curve 2 - InSb [4], curve 3 - InAs [4]

The proper concentration profiles of distribution of donor centers are selected for "stable" regimes of the irradiation for $InSb$ (curve 2 of Fig. 6) and $InAs$ [4].

The difference of absorption indexes for Ruby and CO_2-laser irradiation is caused of the impossibility of laser annealing and activation implanted impurity with the help of the laser irradiation with regimes with $h\nu > E_g$. For the laser annealing of ion-implanted layers must be used the irradiation with with $h\nu < E_g$. The irradiation with $h\nu > E_g$ is the processes of light scattering on stable centers (covalent bonds for $InSb$ and $InAs$ [4]. This process is caused of the generation high concentration of donor centers. Defects of ion implantation have n type of the conductivity too. The thermal defects in $InSb$ have p-type of conductivity [4]. Therefore, the contradiction in the explanation of the cause the creation and annealing damages and activation impurity in $InSb$ is founded on various charge states laser induced damages and thermal defects.

The nature of the ion-implanted annealed impurity is known and has theoretical models [4]. The problem of nature the donor centers in InSb, InAs, Ge and Si is little known and must be researched in detail. In [4] these centers are determined as "dangling" bonds. These "dangling" bonds have various physical properties, which is dependent from the intensity of the irradiation [4]. For the small intensity of the irradiation "dangling" bonds have small life-time from 10^{-7} s for nonequilibrium charges for self-absorption processes to 10^{-2} s for exciton drops [4]. Further increasing of the intensity of the irradiation is

caused the increasing life-time of irreversible changes. In InSb this changes is correlated with changes of the concentration the donor centers [4].

The dynamical change of the concentration subsurface damages in InSb after Ruby laser irradiation is represented in Fig. 6 and curve 2 of Fig. 11.

Among other types of complex treatments, we should note the following:

1. When a magnetic or electric field is applied to the substrate to be sputtered, or a certain mask is applied, as in photolithography (including laser lithography) [5-11].
2. Now let's analyze how black silicon can be obtained by other methods. If we want to miniaturize the procedure (Fig. 3 or Fig. 4), then for the first stage of obtaining black silicon, we can use either laser irradiation (Fig. 7) or ion implantation, the initial nanostructures of black silicon will have a height of 10-50 μm, for this you only need to select the regenerative irradiation mode. Similarly, these procedures can be using for other compounds [29-32].
3. Laser-induced optical breakdown processes can also be using to obtain multilayer radial heterostructures and should be taken into account when increasing the resource of optical information transmission lines [3].

Conclusions

1. Short review the creation of the laser-induced thin films is representing.
2. Main properties pulsed laser deposition thin films are analyzed.
3. Problem of creation surface laser-induced layers in InSb and In As is observed.
4. Questions of creation laser-induced nano and misrostructures in Si and Ge are researched.
5. Main peculiarities of laser-induced optical breakdown in SiC and KCl and its possible application for the receiving surface heterostructures are discussed.
6. Questions about applications laser radiation in the complex technologies (laser annealing of ion implantation of various materials, influence of electrical and magnetic fields on processes of formation laser-induced thin films) are included.

References

1. Trokhimchuck PP. Relaxed optics: modeling and discussions. Saarbrucken: Lambert Academic Publishing; 2020. p. 249.
2. Trokhimchuck PP. Relaxed optics: modeling and discussions 2. Saarbrucken-Cisinau: Lambert Academic Publishing; 2022. p. 210.
3. Trokhimchuck PP. Relaxed optics: modeling and discussions 3. Saarbrucken-Cisinau: Lambert Academic Publishing; 2024. p. 256.
4. Trokhimchuck PP. Foundations of relaxed optics. Lutsk: Volyn University Press; 2011. p. 627.
5. Ashfold MNR, Claeyssens F, Fuge GM, Henley SJ. Pulsed laser ablation and deposition of thin films. Chem Soc Rev. 2004;33:23-31.
6. Benetti D, Nouar R, Nechache R, Pepin H, Sarkissian A, Rosei F, *et al*. Combined magnetron sputtering and pulsed laser deposition of TiO and BFCO thin films. Sci Rep. 2017;7(1):1-9.
7. Ogugua SN, Ntwaeaborwa OM, Swart HC. Latest developments on pulsed laser deposited thin films for advanced luminescence applications. Coatings. 2020;10(11):1078-1099.
8. Sloyan KA, May-Smith TC, Zervas M, Eason RW, Huband S, Walker D, *et al*. Growth of crystalline garnet mixed films, superlattices, and multilayers for optical applications via shuttered combinatorial pulsed laser deposition. Opt Express. 2010;18(24):24679-24688.
9. Sanz M, López-Arias M, Rebollar E, De Nalda R, Castillejo M. Laser ablation and deposition of wide bandgap semiconductors: plasma and nanostructure of deposits diagnosis. J Nanopart Res. 2011;13(12):6621-6631.
10. Kolasinski KW, Gupta MC, Zhigilei LV. Plume and nanoparticle formation during laser ablation. In: Wandelt K, editor. Encyclopedia of interfacial chemistry: surface science and electrochemistry. Oxford: Elsevier; 2018. p. 594-603.
11. Prevosti S. Ablation of Si with femtosecond laser. Stockholm: KTH Royal Institute of Technology; 2016. p. 61.
12. Pedraza AJ, Fowlkes JD, Lowndes DH. Silicon microcolumn arrays growth by nanosecond pulse laser irradiation. Appl Phys Lett. 1999;74(10):2222-2224.

13. Pedraza AJ, Guan YF, Fowlkes JD, Smith DA, Lowndes DH. Nanostructures produced by ultraviolet laser irradiation of silicon. I. Rippled structures. J Vac Sci Technol B. 2004;22(10):2823-2835.
14. Pedraza AJ, Fowlkes JD, Jesse S, Mao C, Lowndes DH. Surface micro-structuring of silicon by excimer-laser irradiation in reactive atmospheres. Appl Surf Sci. 2000;168(1-4):251-257.
15. Shugaev MV, Gnilitskyi I, Bulgakova NM, Zhigilei LV. Mechanism of single-pulse ablative generation of laser-induced periodic surface structures. Phys Rev B. 2017;96(20):205459.
16. Gnilitskyi I, Mamykin SV, Lanara C, Hevko I, Dysheyko M, Bellucci S, et al. Laser nanostructuring for diffraction grating-based surface plasmon resonance sensors. Nanomaterials. 2021;11:591.
17. Katiyar AK, Singha AK, Manna S, Aluguri R, Ray SK. Optical photoresponse of CuS - n-Si radial heterojunction with Si nanocone arrays fabricated by chemical etching. Phys Chem Chem Phys. 2013;15:20887-20993.
18. Sarkar A, Katiyar AK, Mukherjee S, Singh S, Singh SK, Das AK, *et al.* Geometry-controlled light emission and extraction in CdS/Black-Si conical heterojunctions. ACS Appl Electron Mater. 2018;1:25-33.
19. Black silicon [Internet]. Available from: https://en.wikipedia.org/wiki/Black_silicon
20. Yablonovich E. Optical dielectric strength of alkali halide crystals obtained by laser-induced breakdown. Appl Phys Lett. 1971;19(11):495-497.
21. Okada T, Tomita T, Matsuo S, Hashimoto S, Ishida Y, Kiyama S, *et al.* Formation of periodic strain layers associated with nanovoids inside a silicon carbide single crystal induced by femtosecond laser irradiation. J Appl Phys. 2009;106(5):054307.
22. Okada T, Tomita T, Matsuo S, Hashimoto S, Kashino R, Ito T. Formation of nanovoids in femtosecond laser-irradiated single crystal silicon carbide. Mater Sci Forum. 2012;725:19-22.
23. Golub I. Optical characteristics of supercontinuum generation. Opt Lett. 1990;15(6):305-307.
24. Shen M, Carey JE, Crouch CH, Kandyla M, Stone HA, Mazur E *et al.* High-density regular arrays of nano-scale rods formed on silicon surfaces

via femtosecond laser irradiation in water. Nano Lett. 2008;8(7):2087-2091.

25. Bogatyryov VA, Kachurin GA. The creation of low-resistivity n-layers on InSb using impulse laser irradiation. Phys Tech Semicond. 1977;11(1):100-102. Russian.
26. Philips JC. Metastable honeycomb model of laser annealing. J Appl Phys. 1981;52(12):7397-7402.
27. Trokhimchuck PP. To question about nature of laser-induced cavitation. IJARPS. 2023;10(5):1-16.
28. Medvid' A. Nano-cones formed on a surface of semiconductors by laser radiation: technology, model, and properties. In: Lupu N, editor. Nanowires science and technology. Vukovar: Inech; 2010. p. 61-82.
29. Xia Y, Liu B, Liu J, Shen Z, Li C. Novel method to produce black silicon for solar cells. Sol Energy. 2011;85:1574-1578.
30. Singh AK, Gryczynski KG, Park SY, Kim M, Neogi A. Broad band light emission from Ag-ion implanted silicon nanocrystals. Solid State Commun. 2011;151(20):1405-1409.
31. Centre d'elaboration de matriaux et d'etudes structurales CEMES-UPR 8011. Rapport d'activité du CEMES Le Bilan 2005-2009. Toulouse: CEMES; 2009. p. 145.
32. Ryssel H, Ruge I. Ion implantation. New York: John Wiley & Sons; 1986. p. 350.
33. Trokhimchuck PP. Problem of saturation of excitation in relaxed optics. J Optoelectron Adv Mater. 2012;14(3):363-370.
34. Bohr A. Atomic interaction in penetration phenomena. Matematisk-Fysiske Meddelelser. 1948;24(190):1-52.